Nanoscale

Curvature-driven adsorption of cationic nanoparticles to phase boundaries in multicomponent lipid bilayers

Journal:	*Nanoscale*
Manuscript ID	NR-ART-09-2018-007763.R2
Article Type:	Paper
Date Submitted by the Author:	07-Jan-2019
Complete List of Authors:	Sheavly, Jonathan; University of Wisconsin-Madison, Chemical and Biological Engineering Pedersen, Joel; University of Wisconsin, Department of Soil Science Van Lehn, Reid; University of Wisconsin-Madison, Chemical and Biological Engineering

Nanoscale

ARTICLE TYPE

Cite this: DOI: 10.1039/xxxxxxxxxx

Curvature-driven adsorption of cationic nanoparticles to phase boundaries in multicomponent lipid bilayers†

Jonathan K. Sheavly,[a] Joel A. Pedersen,[b] and Reid C. Van Lehn[a]

Received Date
Accepted Date

DOI: 10.1039/xxxxxxxxxx

www.rsc.org/journalname

Understanding the interactions between surface-functionalized gold nanoparticles (NPs) and lipid bilayers is necessary to guide the design of NPs for biomedical applications. Recent experiments found that cationic NPs adsorb more strongly to phase-separated multicomponent lipid bilayers than single-component liquid-disordered bilayers, suggesting that phase separation affects NP-bilayer interactions. In this work, we use coarse-grained molecular dynamics simulations to investigate the effect of lipid phase behavior on the adsorption of small cationic NPs. We first determined the free energy change for adsorbing a NP to one-phase liquid-disordered and one-phase liquid-ordered bilayers. The simulations indicate that NP adsorption depends on a competition between favorable NP-lipid interactions and the unfavorable curvature deformation of the bilayer, resulting in stronger interactions with the liquid-disordered bilayer due to its lower bending modulus. We then measured the free energy change associated with moving a NP across the surface of a phase-separated bilayer and identified a free energy minimum at the phase boundary. The free energy minimum is attributed to the thickness gradient between the two phases that enables favorable NP-lipid interactions without necessitating large curvature deformations. The simulation results thus indicate that the intrinsic curvature present at phase boundaries drives preferential interactions with surface-adsorbed NPs, providing new insight into the forces that drive NP behavior at multicomponent, phase-separated lipid bilayers.

1 Introduction

Gold nanoparticles (NPs) are extensively researched as biocompatible materials for potential applications in diagnostic imaging,[1,2] drug delivery,[3,4] and photothermal therapy.[5,6] NPs are suitable for these applications because their properties can be tuned by independently modifying their size and by grafting ligands to the gold core to dictate chemical properties, such as charge or hydrophobicity.[7–9] This level of synthetic control thus affords a large possible set of surface-functionalized NPs for biological applications, but structure-function relationships between NP properties and NP behavior in biological environments are still largely lacking, inhibiting NP design.

NP interactions with the cell membrane are critically important for biological applications because they can influence cell internalization, cytotoxicity, or NP assembly on the cell surface.[10–12] For example, NP size and surface chemistry modulate NP-membrane adsorption, which can affect the rate and likelihood of endocytosis as a mechanism of activated cell uptake.[11,13] Small amphiphilic NPs have been shown to directly penetrate across the membrane and into cells without undergoing endocytosis, which is useful for applications such as siRNA delivery.[14,15] Conversely, highly charged cationic NPs have been shown to induce cell death, presumably due to the disruption of the membrane.[12,14,16] While these examples illustrate how diverse behaviors depend on NP physicochemical properties, further interrogating NP-membrane interactions experimentally is challenging due to the immense complexity of biological systems.

Alternatively, significant work has focused on characterizing NP interactions with model single-component supported lipid bilayers or lipid vesicles as mimics for cell membranes.[17–23] For example, experimental measurements of NP-bilayer interactions in model systems have shown that hydrophobic and amphiphilic NPs can embed within the hydrophobic core of the bilayer,[24] large cationic NPs can induce the formation of bilayer pores,[16,17] and small, anionic NPs can cluster on the bilayer surface.[25] The simplicity of single-component bilayers also enables comparisons with computational models, such as atomistic or coarse-grained

[a] Department of Chemical and Biological Engineering, University of Wisconsin-Madison, 1415 Engineering Drive, Madison, WI, USA. E-mail: vanlehn@wisc.edu
[b] Departments of Soil Science, Chemistry, and Civil & Environmental Engineering, University of Wisconsin-Madison, 1525 Observatory Drive, Madison, WI, USA.

† Electronic Supplementary Information (ESI) available: details on simulation methods, system preparation, and analysis; convergence of free energy calculations; additional simulation analysis. See DOI: 10.1039/b000000x/

(CG) molecular dynamics (MD) simulations.[26–34] MD simulations have similarly revealed the formation of bilayer pores as a function of NP size and charge,[35] shown the insertion of amphiphilic NPs into the bilayer,[19,36] and investigated cooperative shape changes in the bilayer due to interactions between collections of NPs.[37,38] Such simulations, in conjunction with experiments, have the potential to yield structure-function relationships that can guide NP design.

Despite the widespread use of single-component lipid bilayers as model membrane systems, these simplified models neglect the compositional heterogeneity of cell membranes, which can contain thousands of different lipids, proteins, and glycans.[39] An important example of this compositional heterogeneity is the formation of lipid rafts, which are regions of liquid-ordered (L_o) domains that are surrounded by a liquid-disordered (L_d) continuous phase.[40,41] While the existence, spatial extent, temporal duration, and composition of lipid rafts in biological membranes is debated,[42,43] phase-separated raft-like domains can be reconstituted in model membranes containing a relatively small number of components (typically 3-4). In these model systems, the L_d phase is formed from lipids with unsaturated acyl chains that inhibit lipid packing, while the L_o phase is formed from lipids with saturated acyl chains, which promote lipid packing, and cholesterol, which occupies the free volume between the lipid acyl chains[44] and hydrogen bonds with lipid head groups.[43] The L_o phase has been shown to be more mechanically rigid and thicker than the L_d phase in experimental measurements[45] and in simulation studies[46] due to these composition differences and the resulting increase in lipid tail order.

The distinct compositions and properties of the L_d and L_o phases influence interactions with surrounding materials. Notably, recent experiments have demonstrated that cationic NPs with 4 nm core diameters adsorb more strongly to a multicomponent, phase-separated supported lipid bilayer containing both L_o and L_d phases than to a single-component L_d bilayer, illustrating the impact of phase separation on NP interactions.[47] Prior studies have suggested that this increased adsorption could be due to either preferential interactions with a particular phase or with the phase boundary. For example, the difference in the mechanical properties of L_d and L_o phases has been shown to direct the partitioning of adsorbed NPs[48] and transmembrane proteins.[40] Certain transmembrane proteins, viral fusion peptides, and membrane-embedded hydrophobic or amphiphilic NPs have been shown to preferentially adsorb to the boundary between the two phases.[49,50] The phase boundary has been associated with increased permeability,[51] unusual water structure,[52] and bilayer thickness deformations,[52,53] all factors that potentially drive preferential adsorption.[40] Recent unbiased CG simulations have also demonstrated that hydrophilic NPs diffuse to phase boundaries.[36,54] However, a mechanistic understanding of the driving forces underlying the increased adsorption of cationic NPs to phase-separated raft-like bilayers remains unknown.

In this work, we used MD simulations to model the adsorption of cationic NPs to one-phase L_o and L_d bilayers and to a phase-separated bilayer containing both phases. We employed the CG MARTINI force field,[55] which has been widely used to investigate NP-bilayer interactions,[33,36,56,57] to reach the long time- ($\sim 1\ \mu s$) and length scales ($\sim$10 nm) needed to model adsorption to phase-separated bilayers. To gain insight into the experimental observation of increased NP adsorption to two-phase bilayers, we first calculated the free energy for adsorbing a NP to a one-phase L_d bilayer and a one-phase L_o bilayer. We found that the NP adsorbs more strongly to the one-phase L_d bilayer by inducing curvature to maximize favorable NP-lipid contact. We then calculated the free energy for moving an adsorbed NP between the L_d and L_o domains of a two-phase bilayer and identified a local free energy minimum at the phase boundary due to favorable local curvature. These results provide new insight into how both chemical and physical forces can drive NP adsorption and partitioning in multicomponent, spatially heterogeneous systems that are relevant to the design of NPs for biological applications.

2 Methods

CG MD simulations were performed to quantify the interactions between cationic NPs and both one- and two-phase lipid bilayers. A CG model is needed due to the large system size and long timescales needed to model NP adsorption to phase-separated bilayers. The MARTINI force field[55,57] was used to model lipids and the NP while the big multipole water (BMW) model was used for the solvent.[58,59] We chose the MARTINI force field because it has been previously shown to reproduce the structural properties of phase-separated lipid bilayers[60,61] and it can capture behavior at bilayer interfaces.[33,36,56,57] We chose the BMW model because it more closely reproduces the electrostatic potential near a lipid bilayer measured with atomistic simulations[58] compared to the normal or polarizable MARTINI water model (ESI Fig. S1a), and moreover led to NP-bilayer adsorption behavior in qualitative agreement with experiments (discussed in the Results below and shown explicitly in ESI Fig. S1b).[47] All MD simulations were performed using a leapfrog integrator with a timestep of 20 fs. Simulation parameters were selected to match the BMW parameters and follow general MARTINI suggestions as reported in the ESI.[57,58] Simulations were performed using the GROMACS (version 2016) package.[62]

The NP was modeled as a hollow, spherical shell with a 4 nm diameter. The shell consisted of 240 ligands, each representing a mercaptopropylamine ($MPNH_2$) ligand to mimic the reference experimental system.[47] The number of ligands was chosen to match recent experimental measurements for similar gold NPs.[13] $MPNH_2$ was represented by a cysteine and lysine MARTINI bead to represent the thiol and ammonium groups, respectively (Fig. 1a).[63] The cysteine beads were uniformly distributed across the spherical shell. While previous calculations have suggested that NPs with this core size and ligand density ($\approx$ 4.8 ligands/nm^2) would have approximately 20 neutral ligands at physiological pH due to pKa shifts,[64] we chose to treat all ligand end groups as protonated and positively charged due to the relatively small fraction of ligands affected and due to the uncertainty in the spatial arrangement of neutral ligands, particularly when the NP is near a bilayer.

The unsaturated lipid dilinoleoyl phosphatidylcholine (abbreviated DIPC in the MARTINI force field) was used to emulate

the L_d phase and a 1:1 mixture of the saturated lipid dipalmitoyl phosphatidylcholine (DPPC) and cholesterol (CHOL) was used to emulate the L_o phase following prior work.[60] The CG structures used in the simulation are shown in Fig. 1b and detailed chemical structures are shown in ESI Fig. S2. The one-phase bilayers were generated using the INSANE script[65] and subsequently solvated with BMW water molecules and neutralizing counterions. The initial simulation box size was set to $14 \times 14 \times 24$ nm^3 to ensure that any bilayer perturbations and NP-bilayer interactions decayed prior to the periodic boundaries (ESI Fig. S3). Simulation snapshots of each one-phase bilayer with an adsorbed NP are shown in Fig. 1c. The two-phase bilayer was generated by combining a 1:1 ratio of the L_d and L_o phases, since Davis *et al.* have shown that this composition phase-separates on a timescale of 2 μs.[61] The initial simulation box size was set to $15 \times 34 \times 17$ nm^3 to ensure that each phase was large enough to exhibit the same properties as in the one-phase bilayers and to ensure that any bilayer perturbations decayed prior to the periodic boundaries (ESI Fig. S4). A simulation snapshot of a two-phase bilayer with an adsorbed NP is shown in Fig. 1d. Additional details on system preparation, a list of system components, and justification for each system size are included in the ESI.

For each of the one-phase bilayers, we performed umbrella sampling to measure the potential of mean force (PMF) for adsorbing the NP to the bilayer surface. We used the z-component of the distance between the NP center of mass (COM) and the bilayer COM as the reaction coordinate (see axes in Fig. 1d). This distance is defined as $D_{z,\mathrm{NP}}$. Umbrella sampling was performed using 55 windows for the L_o bilayer and 60 windows for the L_d bilayer spaced by 0.1 nm along the reaction coordinate, then the Weighted Histogram Analysis Method (WHAM) was used to compute the PMF.[66] Each window was equilibrated for 55 ns followed by 100 ns of production. Simulations were performed at 295 K (to match the two-phase simulations described below) using a Berendsen thermostat and 1 bar using a semi-isotropic Berendsen barostat with a 3×10^{-5} bar^{-1} compressibility.[58]

For the two-phase bilayer, we performed umbrella sampling to measure the PMF for moving an adsorbed NP between the two phases. We used the y-component of the distance between the NP COM and the COM of the L_o phase as the reaction coordinate (see axes in Fig. 1d). This distance is defined as $D_{y,\mathrm{NP}}$. The system was equilibrated for 20 ns prior to NP adsorption. Umbrella sampling was performed using 144 windows spaced by 0.1 nm along the reaction coordinate, then WHAM was used to compute the PMF. Initial configurations for each window were generated by moving the adsorbed NP across the lipid bilayer with the lipids restrained to inhibit any disruption of lipids during the pulling process. Each window was then equilibrated for 100 ns followed by 150 ns of production. Simulations were performed at 295 K (to maintain two-phase coexistence[61]) using a Berendsen thermostat and 1 bar using an anisotropic Berendsen barostat with a 3×10^{-5} bar^{-1} compressibility in the x and z directions and a fixed box size in the y direction. The two-phase bilayer was also simulated in the absence of the NP for 200 ns in the same ensemble to evaluate its equilibrium properties. Under these conditions, two-phase coexistence with a well-defined phase boundary was maintained in all simulations.

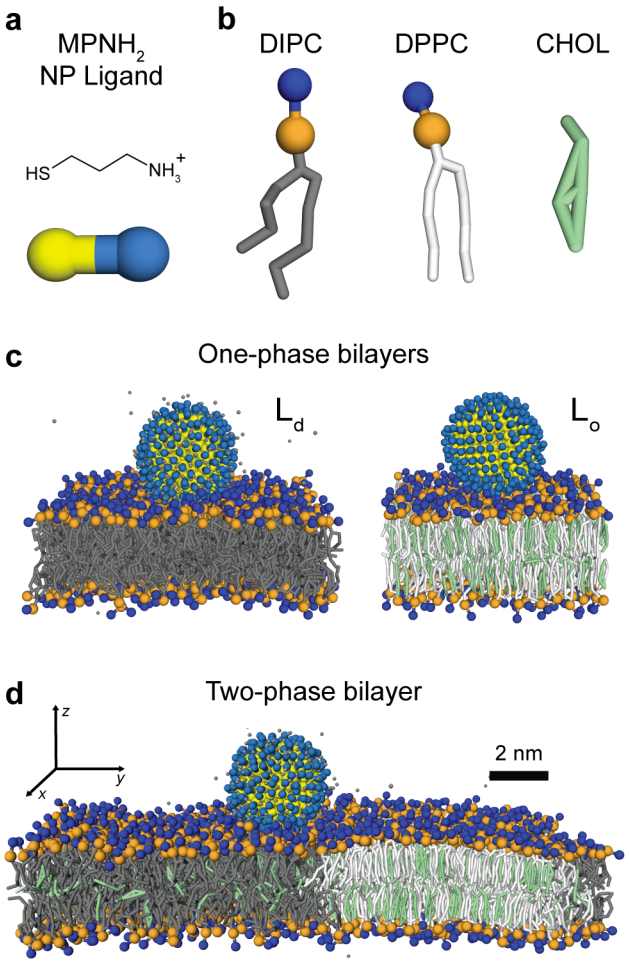

Fig. 1 Snapshots of relevant structures. **a)** The nanoparticle (NP) ligand and corresponding chemical structure. **b)** Bilayer components (structures in ESI). **c)** The one-phase liquid-disordered (L_d) and liquid-ordered (L_o) bilayers with adsorbed NPs. **d)** The two-phase bilayer with an adsorbed NP.

Additional details on the umbrella sampling workflow for all bilayers are discussed in the ESI. We performed extensive analysis to confirm the robustness and reproducibility of simulation findings with respect to variations in runtime parameters and initial configurations and to demonstrate that all PMFs converge within the stated sampling time (ESI Figs. S5-S7). Error bars presented in the Results report the standard deviation between two 50-ns blocks for the simulations of one-phase bilayers and two 75-ns blocks for the simulations of two-phase bilayers. In total, nearly 100 μs of simulations were performed.

3 Results

3.1 NP adsorption free energies for one-phase bilayers

NP-bilayer adsorption free energies were first calculated independently for one-phase L_d and L_o bilayers. Fig. 2 plots the PMF as a function of $D_{z,\mathrm{NP}}$ for each of the two bilayers. A value of 0 corresponds to a NP positioned in aqueous solution 9.5-10 nm from the bilayer center. Each PMF exhibits a pronounced free energy min-

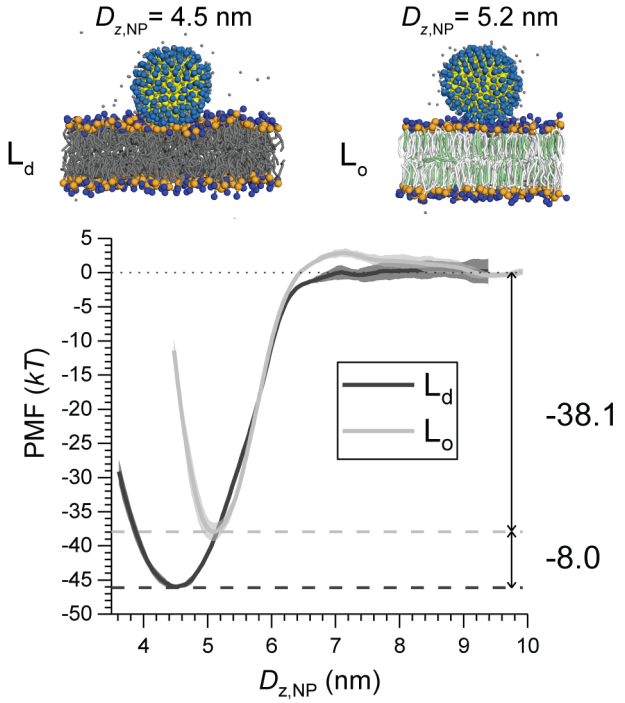

Fig. 2 Potential of mean force (PMF) for nanoparticle (NP) adsorption to each one-phase bilayer as a function of the z-component of the distance between the center of mass (COM) of the bilayer and the COM of the NP ($D_{z,NP}$). The simulation snapshots at top show representative configurations at the values of $D_{z,NP}$ corresponding to the PMF minima. The shaded area around each curve indicates the standard deviation computed by dividing the trajectory into two blocks.

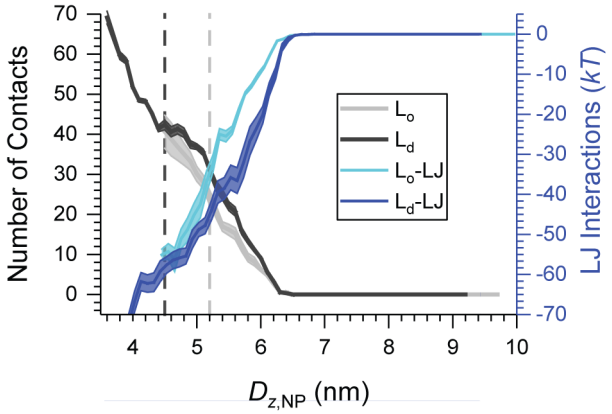

Fig. 3 The number of nanoparticle (NP) contacts with lipid head groups as a function of the z-component of the distance between the center of mass (COM) of the bilayer and the COM of the NP ($D_{z,NP}$) compared to the total Lennard-Jones (LJ) interaction between the NP and the bilayer. Results are shown for both the one-phase liquid-disordered (L_d) and liquid-ordered (L_o) bilayers. The dashed vertical lines denote the values of $D_{z,NP}$ that correspond to the potential of mean force minima (L_o in grey, L_d in black) shown in Fig. 2. The shaded area around each curve indicates the standard deviation computed by dividing the trajectory into two blocks.

imum of -46.1 kT at $D_{z,NP} = 4.5$ nm and -38.1 kT at $D_{z,NP} = 5.2$ nm for the L_d and L_o bilayers, respectively. The deep free energy minima indicate that the cationic NPs favorably adsorb to both phases; this result qualitatively agrees with experimental findings indicating that similar NPs adsorb to supported lipid bilayers.[47] We predict favorable adsorption with MARTINI simulations using the BMW water model but not with MARTINI simulations with the polarizable water model, which predict purely repulsive behavior (ESI Fig. S1b), further justifying the model representation. By comparing the PMF minima, the simulations show that the NP adsorbs more strongly to the L_d bilayer than the L_o bilayer by 8.0 $\pm$ 1.3 kT. This result suggests that the experimental observation of increased NP adsorption to phase-separated supported lipid bilayers[47] cannot be explained by preferential NP adsorption to the L_o phase alone.

3.2 NP interactions with lipid head groups drive adsorption

We next analyzed the interactions driving adsorption to understand the differences between the two PMF profiles. Fig. 3 shows the Lennard-Jones (LJ) interactions between the NP and each one-phase bilayer. The LJ interactions decrease monotonically as the NP-bilayer distance decreases for both systems, with the onset of LJ attraction coinciding with the decrease in the PMF. LJ interactions between the NP and lipids in the L_d bilayer are stronger than LJ interactions with the L_o bilayer; at the distances corresponding to the PMF minima, the LJ interactions are -57.6 and -36.7 kT for the L_d and L_o bilayer, respectively. The similarity in magnitude between the PMF minima and the magnitude of the LJ interactions at corresponding distances suggests that LJ interactions are the dominant attractive component for each PMF. Note that van der Waals and hydrogen bonding interactions are both represented by LJ interactions in the MARTINI force field[55,57] so we cannot distinguish between these contributions without more detailed simulations.

The increase in LJ attraction as $D_{z,NP}$ decreases can either be attributed to an increase in the number of interactions between the zwitterionic lipid head groups and the NP surface or stronger interactions between the nonpolar acyl chains of the lipids and the NP surface, although the latter possibility is unlikely due to the absence of hydrophobic beads on the NP. We quantified the number of NP-lipid contacts by counting the average number of lipid head groups within a 3.5 nm cutoff radius of the NP COM; this value is the sum of the NP radius, approximate ligand length, and the standard diameter of a MARTINI CG bead. Fig. 3 shows the number of NP-lipid contacts as a function of $D_{z,NP}$. There is a similar monotonic increase in the number of contacts between the NP and both one-phase bilayers with decreasing $D_{z,NP}$, but at the PMF minimum there are more contacts with the L_d bilayer compared to the L_o bilayer. We further confirmed that the magnitude of the LJ interactions and the number of NP-lipid contacts are linearly correlated (ESI Fig. S8), indicating that the deeper PMF minimum observed for the L_d bilayer is due to additional NP-lipid interactions that lead to stronger LJ attraction.

3.3 Bilayer curvature facilitates adsorption to the L_d phase

The results of Fig. 3 do not resolve why there are more NP-lipid contacts for the L_d bilayer. Maximizing the number of NP-lipid contacts induces local bilayer curvature (visible in Fig. 2a) due to the curvature of the NP surface, which incurs an elastic free energy penalty that depends on the bending modulus of the bilayer. Since the L_o phase has a larger bending modulus than the L_d phase,[46,67,68] the difference in the number of contacts (and thus the LJ interactions) may be due to the mechanical properties of each phase. Assuming that the bilayer acts as a thin elastic sheet, the free energy penalty associated with inducing bilayer curvature, ΔG_{curve}, is obtained from continuum theory as:[69]

$$\Delta G_{\text{curve}} = \frac{1}{2}\int_A \mathrm{K_c}\,[H(x,y) - H_0(x,y)]^2 \mathrm{d}A \qquad (1)$$

where $H(x,y)$ is the mean bilayer curvature at a given x and y coordinate, $H_0(x,y)$ is the intrinsic bilayer curvature prior to NP adsorption, $\mathrm{K_c}$ is the bending modulus, and A is the surface area of the bilayer.[70] In order to simplify this expression, we employ the small gradient approximation to approximate the mean curvature as the Laplacian of the bilayer height:[69]

$$H(x,y) \approx \nabla^2 h(x,y) \qquad (2)$$

$$H_0(x,y) \approx \nabla^2 h_0(x,y) \qquad (3)$$

We approximated the height profiles, $h(x,y)$ and $h_0(x,y)$, as the z-component of the distance between the lipid phosphate groups and the COM of the bilayer and applied a Gaussian kernel function to transform the discrete lipid positions into a differentiable surface. We then numerically evaluated the Laplacian of the entire bilayer (including both leaflets) with the NP to obtain $\nabla^2 h(x,y)$ and without the NP to obtain $\nabla^2 h_0(x,y)$ and calculated the integral numerically. Bending moduli were estimated as $\mathrm{K_c} = 26\ kT$ for the L_d phase and $\mathrm{K_c} = 64\ kT$ for the L_o phase based on prior measurements using the MARTINI force field.[46] Complete details on this procedure are included in the ESI.

Fig. 4a shows ΔG_{curve} as a function of $D_{z,\text{NP}}$ for both one-phase bilayers. As the NP approaches the bilayer (*i.e.*, as $D_{z,\text{NP}}$ decreases) ΔG_{curve} increases for both bilayers as curvature is induced. The increase in ΔG_{curve} coincides with the initiation of NP-bilayer contacts in Fig. 3. For the L_d bilayer, ΔG_{curve} reaches a local maximum at $D_{z,\text{NP}}$=5.7 nm, decreases to a local minimum that coincides with the PMF minimum at $D_{z,\text{NP}} = 4.5$ nm shown in Fig. 2, then increases monotonically for smaller values of $D_{z,\text{NP}}$. Similar behavior is observed for the L_o bilayer, although ΔG_{curve} increases more rapidly for values of $D_{z,\text{NP}}$ that are smaller than the value $D_{z,\text{NP}}$ at the PMF minimum. ΔG_{curve} is approximated as 5.8 kT and 12.5 kT for the L_d and L_o bilayer, respectively, at the values of $D_{z,\text{NP}}$ corresponding to the PMF minima.

The non-monotonic behavior of ΔG_{curve} observed for the L_d bilayer can be explained by analyzing the bilayer height near the NP. Fig. 4b shows average values of $h(x,y)$ for the L_d bilayer as a function of the radial distance from the NP, $D_{r,\text{NP}}$, at various values of $D_{z,\text{NP}}$. The curve in dark blue corresponds to the value of $D_{z,\text{NP}}$ at the PMF minimum, curves shaded in green indicate values of $D_{z,\text{NP}}$ larger than the value at the PMF minimum, and

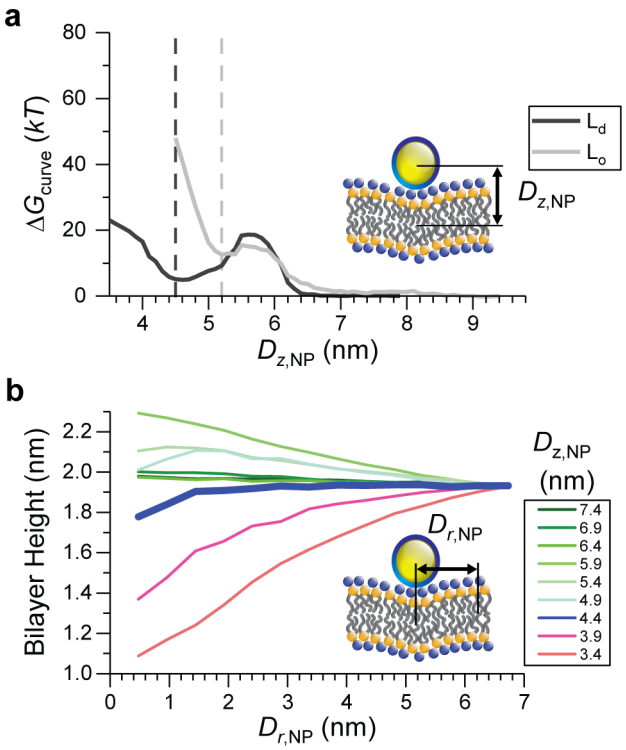

Fig. 4 Curvature induced by nanoparticle (NP) adsorption to one-phase bilayers. **a)** The change in the curvature free energy, ΔG_{curve}, as a function of the z-component of the distance between the center of mass (COM) of the bilayer and the COM of the NP ($D_{z,\text{NP}}$) for each one-phase bilayer. The dashed vertical lines indicate the values of $D_{z,\text{NP}}$ at the potential of mean force (PMF) minima in Fig. 2. **b)** The average bilayer height as a function of the radial distance from the NP ($D_{r,\text{NP}}$) for the liquid-disordered bilayer. Each curve corresponds to a different value of $D_{z,\text{NP}}$. The curve corresponding to the minimum of the PMF in Fig. 2 is shown as a bold, blue line.

curves shaded in red indicate values of $D_{z,\text{NP}}$ smaller than the value at the PMF minimum. The bilayer is flat at large values of $D_{z,\text{NP}}$ (when the NP is far from the bilayer). As $D_{z,\text{NP}}$ decreases, the bilayer height increases radially around the NP to initiate NP-lipid contacts, leading to positive bilayer curvature and the local maximum in ΔG_{curve}. This induced curvature is possible only due to the relative flexibility of the L_d bilayer and is suppressed for the L_o bilayer (ESI Fig. S11). As $D_{z,\text{NP}}$ further decreases, the induced curvature becomes negative due to the curvature of the NP core. At the PMF minimum, the bilayer exhibits slight negative curvature corresponding to the local minimum in ΔG_{curve}. Further decreases in $D_{z,\text{NP}}$ lead to large increases in curvature consistent with large increases in ΔG_{curve}. This analysis indicates that negative curvature maximizes the number of NP-lipid contacts; similar negative curvature is also induced at the PMF minimum for the L_o phase (ESI Fig. S11).

3.4 Competition between NP-lipid interactions and induced curvature

The preceding results suggest that a competition between favorable LJ interactions and unfavorable curvature free energies leads

to the behavior of the PMFs in Fig. 2. For the L_d bilayer, the sum of the LJ interactions and ΔG_{curve} at $D_{z,NP}$=4.5 nm, corresponding to the minimum of the PMF, is -51.8 kT, which is in reasonable agreement with the -46.1 kT PMF minimum. For the L_o bilayer, the sum of the LJ interactions and ΔG_{curve} at $D_{z,NP}$=5.2 nm, corresponding to the minimum of the PMF, is -24.2 kT, which differs more significantly from the -38.1 kT PMF minimum. This comparison suggests that alternative interactions, such as solvent-mediated or electrostatic interactions, could contribute to the difference between the PMF and the sum of the LJ interactions and ΔG_{curve} for the L_o bilayer, although some of the disagreement for both comparisons may be due to the error in the LJ interactions, approximations made in the ΔG_{curve} calculation, or inaccurate estimates of K_C. Nonetheless, the favorable agreement between this sum and the PMF minimum for the L_d bilayer suggests that trends in adsorption behavior can be predicted with these quantities.

The study of the one-phase bilayers indicates that favorable NP-lipid contacts drive NP adsorption but induce bilayer curvature and a corresponding elastic energy penalty. Because the bending modulus of the L_d phase is lower than the bending modulus of the L_o phase, the free energy penalty for inducing this preferred curvature is lower for the L_d phase, leading to the stronger adsorption affinity between the NP and L_d phase. Based on this competition between driving forces, we predict that a system which has an intrinsic negative curvature would enable favorable NP-lipid contacts without an additional elastic penalty, yielding favorable NP adsorption. Since a common feature of lipid rafts is a thickness difference between the thinner L_d phase and thicker L_o phase, we thus hypothesize that the cationic NP will preferentially interact with the boundary between phases in a phase-separated raft-like bilayer, as we examine below.

3.5 NP adsorption free energy for the two-phase bilayer

We first calculated the properties of the two-phase bilayer in the absence of a NP. Fig. 5a shows the bilayer height and composition as a function of D_y, which we define as the y-component of the distance from the COM of the L_o phase. The simulation snapshot is to scale and visually indicates the changes in bilayer height and composition. The composition is plotted as the mole fraction of each of the three bilayer components. The L_o phase is enriched in DPPC and CHOL, while the L_d phase is enriched in DIPC and contains a small amount of CHOL (≈10%). The phase boundary corresponds to the region where the composition smoothly transitions between the two phases and is shaded in blue in Fig. 5. Vertical dashed lines indicate the local minimum and local maximum of the PMF in Fig. 5b, as discussed below. The bilayer height is computed by measuring $h_0(x,y)$ and averaging over values along the x-axis. The height smoothly varies between the two phases, thereby generating curvature in the boundary region. The 0.25 nm difference in height between the two phases is consistent with AFM experiments that measured a difference in height of 0.25-0.5 nm.[47,52] The sigmoidal change in bilayer height is similar to the radial height profiles shown in Fig. 4b, suggesting that the phase boundary may promote favorable adsorption. ESI Fig. S7 plots the same quantities computed in the presence of an adsorbed NP to confirm that NP adsorption does not disrupt these structural features.

We next computed the PMF for moving a NP across the phase boundary to determine the preference of the NP for the boundary compared to the two phases. Fig. 5b shows the PMF as a function of $D_{y,NP}$. The plot is shaded according to the bilayer composition shown in Fig. 5a and the PMF is shifted so that a value of zero corresponds to a NP adsorbed to the L_d phase; ESI Fig. S7 confirms that the location of the boundary is not affected by the presence of the NP and is located at consistent values of $D_{y,NP}$. There is a 3.5 kT free energy minimum at $D_{y,NP}$=-9.7 nm, corresponding to the interface of the L_d phase and the phase boundary, and a 5.8 kT free energy maximum $D_{y,NP}$=-5.1 nm, corresponding to the interface of the L_o phase and the phase boundary. The PMF obtains nearly equal values at $D_{y,NP}$=0 nm and $D_{y,NP}$=-14 nm, corresponding to the L_o and L_d phases, respectively. Bulk L_o phase behavior is expected between $D_{y,NP}$=-2 nm and $D_{y,NP}$=0 nm based on Fig. 5a; the small variation in the PMF in this region can be attributed to corresponding variations in bilayer order parameters (Fig. 5a and ESI Fig. S4). The composition of the L_d phase is also not the same as the one-phase L_d bilayer because it contains 10 % cholesterol, which decreases the magnitude of the NP adsorption free energy by 8.3 kT (ESI Fig. S12). This cholesterol content explains why the difference in free energy between the L_o and L_d phases is nearly zero in the two-phase bilayer even though there is a 8.0 kT difference in the NP adsorption free energy to each separate one-phase bilayer (Fig. 2). The agreement between the one-phase adsorption free energies and the two-phase PMF when accounting for cholesterol content further indicates that the two-phase bilayer correctly reproduces bulk phase behavior at limiting values of the reaction coordinate. Finally, we note that there is more error in the PMF and associated quantities for the two-phase bilayer than the one-phase bilayers, which we attribute to bilayer undulations described below.

3.6 Intrinsic curvature determines NP interactions at the phase boundary

The features of the two-phase PMF can be analyzed in terms of the competition between NP-lipid contact and induced bilayer curvature that was identified from the study of the one-phase bilayers. Fig. 6a shows the value of $D_{z,NP}$ as a function of $D_{y,NP}$. The plot is shaded according to the compositions identified in Fig. 5a and vertical dashed lines indicate the local minimum and maximum of the PMF in Fig. 5b. This data shows that the NP adsorbs to the bilayer at values of $D_{z,NP}$ similar to the values of $D_{z,NP}$ that correspond to PMF minima in Fig. 2 for the two individual phases ($D_{z,NP}$ = 4.5 nm for the L_d phase and $D_{z,NP}$ = 5.2 nm for the L_o phase), with $D_{z,NP}$ transitioning between these limiting values in the phase boundary. Fig. 6b shows the number of NP-lipid contacts and LJ interactions between the NP and the bilayer as a function of $D_{y,NP}$. The L_d phase has stronger LJ interactions than the L_o phase, as expected, with a sigmoidal increase across the boundary. The minimum of the PMF corresponds to the value of $D_{y,NP}$ where the LJ interactions reach a local minimum value, while the local maximum of the PMF corresponds to the value

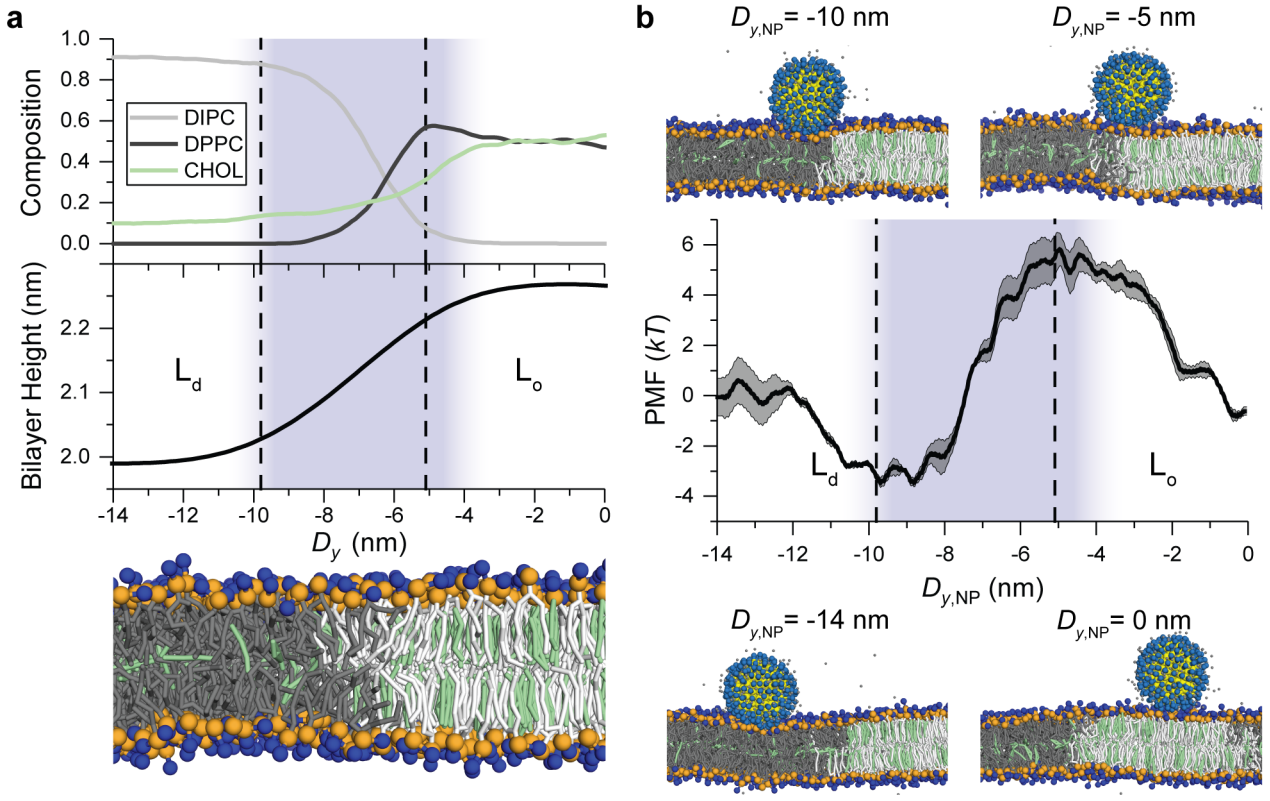

Fig. 5 Properties of the two-phase bilayer and its interaction with a nanoparticle (NP). **a)** The composition and height of the two-phase bilayer in the absence of a NP as a function of the y-component of the distance from the center of mass (COM) of the liquid-ordered phase (D_y). The composition is used to define regions corresponding to the two phases; the two phases are labeled and the boundary is shaded in blue. A simulation snapshot of a two-phase bilayer (to scale) without an adsorbed NP is shown below for reference. **b)** The potential of mean force (PMF) for moving an adsorbed NP across the two-phase bilayer as a function of the y-component of the distance between the COM of the liquid-ordered phase and the COM of the NP ($D_{y,\mathrm{NP}}$). The shaded area around the curve indicates the standard deviation computed by dividing the trajectory into two blocks. Simulation snapshots are shown for characteristic points along the PMF. The dashed vertical lines are shown to designate the minimum and maximum for the PMF and phase boundary is shaded in blue.

of $D_{y,\mathrm{NP}}$ where the LJ interactions reach a local maximum value. The fluctuations in the LJ interactions for values of $D_{y,\mathrm{NP}}$ corresponding to the $\mathrm{L_o}$ and $\mathrm{L_o}$ phases are largely negligible within the error bars. Trends in the number of NP-lipid contacts mirror the trends in the LJ interactions and are numerically similar to the results for the one-phase bilayers (Fig. 3), confirming that in the two-phase bilayer increased NP-lipid contacts again drive increased LJ attraction.

The curvature free energy, $\Delta G_{\mathrm{curve}}$, in the two-phase bilayer is estimated by computing the bending modulus at a particular value of $D_{y,\mathrm{NP}}$ as a weighted average of the modulus of each individual phase based on the mole fraction, as further described in the Supporting Information. A similar approach has been used previously to estimate the elastic moduli of mixed surfactant monolayers,[71] and prior neutron scattering experiments have found that the bending moduli of lipid domains in phase-separated bilayers are similar to the moduli of one-phase bilayers.[67] In the two-phase system, the $H_0(x,y)$ term in Equation 1 varies spatially due to the thickness difference between the two phases, implying that the degree to which the NP deforms the bilayer also depends on spatial position.

Fig. 6c estimates the contribution to $\Delta G_{\mathrm{curve}}$ due to local induced curvature as a function of $D_{y,\mathrm{NP}}$, with shading and vertical dashed lines indicating features from Fig. 5 as described previously. We compute the local induced curvature by integrating Equation 1 over a circular area with a radius of 4.0 nm centered on the NP; this length scale is chosen based on the decay of the induced curvature in the one-phase bilayer (Fig. 4). The local value of $\Delta G_{\mathrm{curve}}$ agrees with expectations, as the minimum of $\Delta G_{\mathrm{curve}}$ corresponds to a value of $D_{y,\mathrm{NP}}$ at the interface of the $\mathrm{L_d}$ phase and the phase boundary. The intrinsic curvature is already negative at this location (Fig. 5a) and thus the NP can maximize attractive interactions without inducing curvature in the y-direction orthogonal to the phase boundary, although some curvature will be induced in the x-direction parallel to the phase boundary. Conversely, the maximum of $\Delta G_{\mathrm{curve}}$ corresponds to a value of $D_{y,\mathrm{NP}}$ at the interface of the $\mathrm{L_o}$ phase and the phase boundary. At this location, the local curvature is positive in the direction orthogonal to the phase boundary so the NP must induce the largest change in local curvature to increase favorable NP-lipid contacts. These features largely mirror the features of the PMF shown in Fig. 5b. Moreover, $\Delta G_{\mathrm{curve}}$ differs by approximately 3-5 kT between the $\mathrm{L_d}$ and $\mathrm{L_o}$ phase, again capturing similar behavior as in the one-phase bilayers (Fig. 4a).

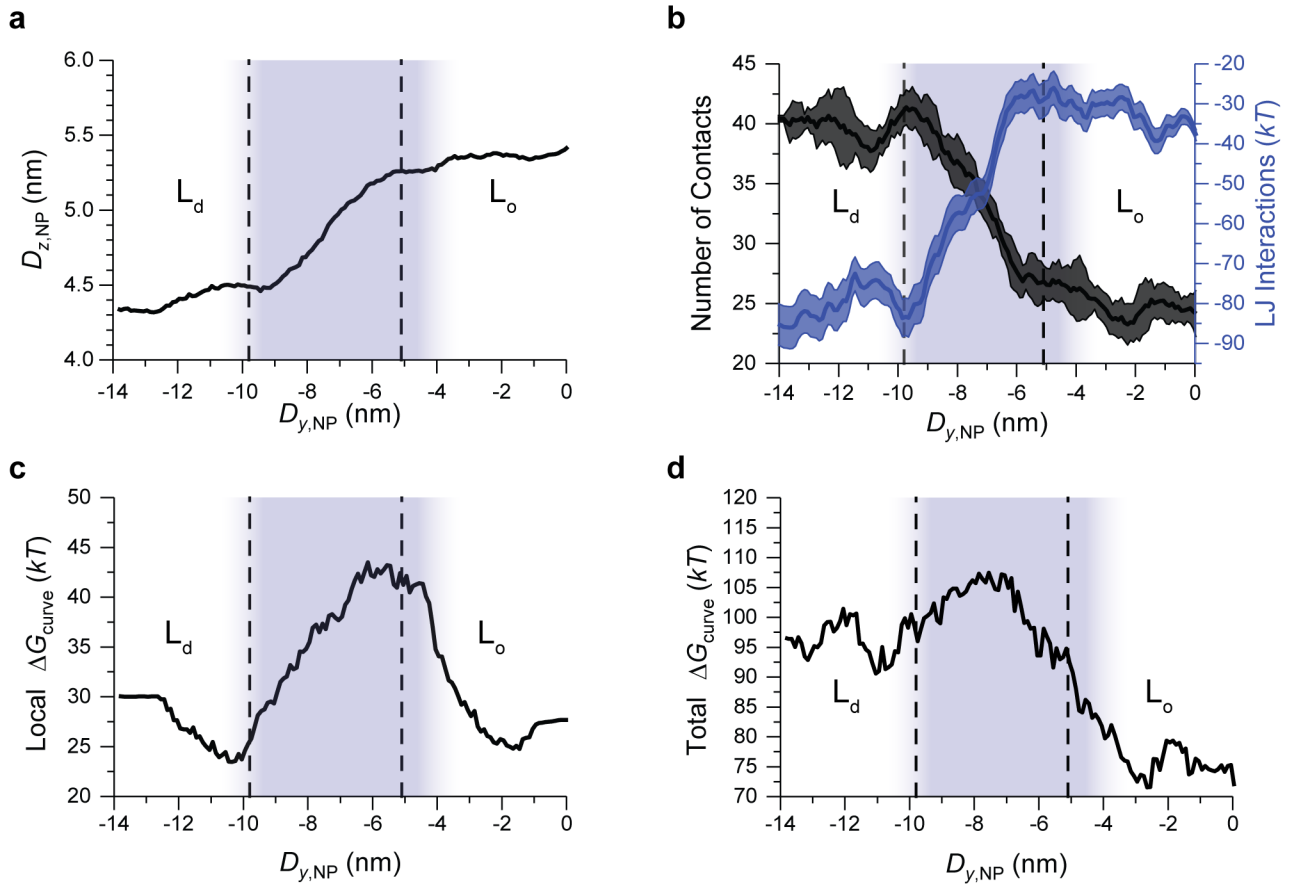

Fig. 6 Driving forces for NP adsorption to the two-phase bilayer as a function of the y distance between the COM of the raft and the COM of the NP ($D_{y,NP}$). Plots are shaded following the same scheme as Fig. 5 and the dashed vertical lines indicate the PMF minimum and maximum. **a)** The z-component of the distance between the COM of the two-phase bilayer and the COM of the NP ($D_{z,NP}$). **b)** Number of contacts and LJ interactions between the NP and the two-phase bilayer. The shaded area around each curve indicates the standard deviation computed by dividing the trajectory into two blocks. **c)** The curvature free energy induced by the NP, computed within a circular area with a radius of 4.0 nm centered on the NP. **d)** The curvature free energy induced by the NP, computed for the entire bilayer.

The results of Fig. 6a-c suggest the following interpretation of PMF features (illustrated by representative simulation snapshots in Fig. 5b). A NP located in the L$_d$ phase ($D_{y,NP} \approx -14$ nm) induces curvature in the bilayer to maximize attractive NP-lipid head group interactions, leading to a larger curvature free energy penalty but strong LJ interactions. A NP located at the interface of the phase boundary and the L$_d$ phase ($D_{y,NP} \approx -10$ nm) can still maximize attractive LJ interactions while inducing less curvature because the intrinsic thickness difference between the two phases leads to local negative curvature. The reduced value of ΔG_{curve} leads to a local minimum in the PMF at this position. A NP located at the interface of the phase boundary and the L$_o$ phase ($D_{y,NP} \approx -5$ nm) is near a region with a larger bending modulus and positive intrinsic curvature. As a result, the number of NP-lipid head group interactions is decreased while the curvature free energy is high, leading to the local maximum in the PMF. Finally, a NP located in the L$_o$ phase ($D_{y,NP} \approx 0$ nm) no longer induces significant curvature, leading to weak LJ attraction but also a small curvature free energy.

3.7 Effect of bilayer undulations on PMF contributions

Fig. 6b and Fig. 6c indicate that the LJ interactions between the L$_d$ and L$_o$ phase differ by approximately -45 kT and ΔG_{curve} differs by approximately 5 kT, but the PMF in Fig. 5b suggests that the total free energy difference between these two phases should be nearly zero. To partially explain this discrepancy, Fig. 6d plots ΔG_{curve} computed by integrating across the total bilayer area, rather than just a local area near the NP. This plot shows distinct features from Fig. 6c: there is a large value of ΔG_{curve} when the NP is located at the L$_d$ phase, a local maximum when the NP is located at the phase boundary, and then a smaller value of ΔG_{curve} when the NP is located at the L$_o$ phase. The total ΔG_{curve} differs by approximately 25 kT between the two phases, thus significantly offsetting the difference in LJ interactions such that the sum of the LJ interactions and ΔG_{curve} differs by 20 kT between the two phases. This difference is comparable to the difference between the sum of the LJ interactions and ΔG_{curve} and the PMF minimum computed for the one-phase L$_o$ bilayer, suggesting that solvent-mediated or electrostatic interactions or error the in the estimate of K_C may again contribute to the remaining difference.

The difference between the local and total values of ΔG_{curve}

emerge from large scale bilayer undulations that lead to changes in the bilayer curvature far from the NP; examples of these curvature changes are illustrated in ESI Fig. S11. Undulations are only observed in the y-dimension (the elongated dimension of the bilayer). Pronounced undulations occur when the NP is adsorbed to the L_d phase or the phase boundary, leading to the large values of ΔG_{curve} in Fig. 6d, which we attribute to the rotation of the rigid L_o phase. While the influence of these undulations on ΔG_{curve} can explain the difference in the measured PMF, we expect that undulations lead to artificially large values of ΔG_{curve} because the finite size of the L_o phase in the simulation system likely contributes to more pronounced rotation than would be observed for the μm-size L_d domains observed experimentally.[47] Moreover, rotation of the L_o phase induces compensating curvature in the L_d phase due to the constraints of the periodic boundary conditions that may instead relax in a much larger system. Because the change in the total ΔG_{curve} across the phase boundary suppresses the difference between the PMF minimum and maximum, we thus suggest that the magnitudes of the PMF maximum and minimum are underestimated due to simulation constraints, while the behavior of the local ΔG_{curve} reported in Fig. 6c more accurately reflects the behavior in the experimental system.

4 Discussion

The CG simulations performed in this study show that cationic NPs favorably adsorb to zwitterionic lipid bilayers in agreement with experimental observations. Adsorption depends on the competition between favorable NP-lipid interactions, which are maximized by negative bilayer curvature, and the unfavorable elastic free energy associated with inducing curvature. This competition leads to preferential NP adsorption to a one-phase L_d bilayer since its lower bending modulus facilitates increased curvature to maximize NP-lipid interactions compared to a one-phase L_o bilayer. These findings are schematically shown in Fig. 7a. NP adsorption to phase-separated raft-like bilayers, in which there is gradient in thickness between the two phases that leads to intrinsic curvature at the phase boundary, can then be interpreted in terms of these findings. The negative intrinsic curvature at the interface of the phase boundary and the L_d phase maximizes attractive NP-lipid interactions, leading to a local PMF minimum. Conversely, the intrinsic curvature at the interface of the phase boundary and the L_o phase is positive and the bending modulus is high, leading to a large elastic free energy penalty, fewer NP-lipid interactions, and a local PMF maximum. Taken together, these findings suggest that NPs that initially adsorb to the L_d phase should partition to the phase boundary due to the local free energy minimum while NPs that initially adsorb to the L_o phase may be excluded from the boundary due to the local free energy maximum. These findings are illustrated in Fig. 7b.

Our results can be used to interpret prior experiments in which cationic NPs were found to adsorb more strongly to a phase-separated supported lipid bilayer than to a one-phase L_d supported lipid bilayer.[47] The present work suggests that these observations are not due to preferential NP adsorption to the L_o phase itself, which is only present in the two-phase bilayer. Instead, preferential adsorption of the NP to the phase boundaries

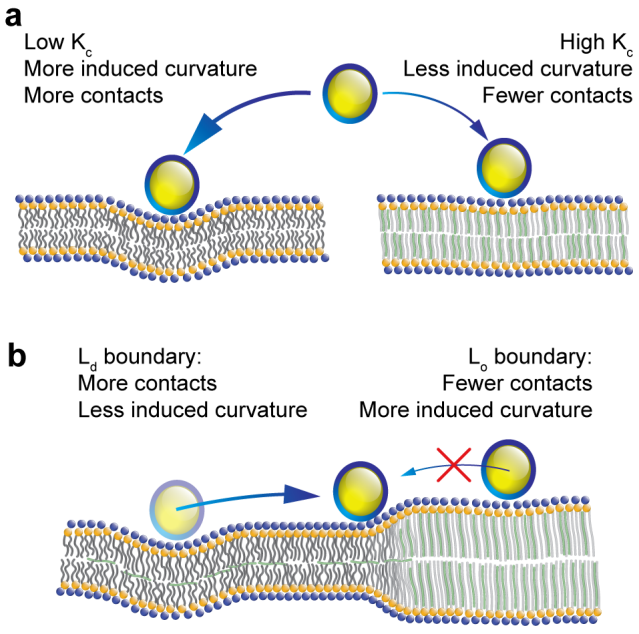

Fig. 7 Schematic representation of simulation findings. **a)** Cationic nanoparticles (NPs) more strongly adsorb to a one-phase liquid-disordered (L_d) bilayer than a one-phase liquid-ordered (L_o) bilayer because the lower bending modulus (K_c) of the L_d phase facilitates induced curvature that maximizes NP-bilayer contact. **b)** Cationic NPs that first adsorb to the L_d phase of a two-phase bilayer preferentially adsorb to the phase boundary where the intrinsic bilayer curvature is negative. NPs that first adsorb to the L_o phase must overcome a free energy barrier due to a region of the boundary that has positive intrinsic curvature.

in the two-phase bilayer could increase NP adsorption compared to a one-phase bilayer lacking any boundaries. However, the local minimum in the PMF presented in Figure 5b is small compared to the adsorption free energies presented in Fig. 2 and the small amount of CHOL in the L_d phase of the two-phase bilayer inhibits adsorption compared to the one-phase bilayer. These findings thus do not provide strong quantitative evidence to explain the experimental results, although it is possible that the MARTINI model may overestimate the magnitude of LJ attractions and underestimate curvature and entropic effects. We also note that the bilayer undulations observed in the simulations may lead to an underestimate of the PMF minimum; such undulations may also be suppressed by the substrate in the supported lipid bilayer studied experimentally, further minimizing this contribution to ΔG_{curve}.

Despite these simulation limitations, the qualitative finding that NP adsorption is favored at the phase boundary is supported by prior experimental results in related systems. For example, HIV peptides and protein toxins have been both shown to adsorb to lipid phase boundaries,[49,50] which may be due to the curvature effects identified here. Similarly, certain peripheral membrane proteins are also known to be sensitive to bilayer curvature which can drive their distribution on the membrane.[72] Future experimental work will be needed to confirm preferential interactions of NPs with lipid phase boundaries based on the simulation predictions presented in this work. Finally, we note that the competition between NP-lipid contacts and induced curvature may also apply

to bilayers in the gel phase as well as the L_o phase; supporting this point, cationic NPs have been observed to adsorb more strongly single-component lipid bilayers at a temperature below the lipid melting point.[73]

The results from this study are in good agreement with other computational studies of NP interactions with phase-separated bilayers. Recently, hydrophilic ligand-coated NPs were shown to adsorb near the phase boundary of two-phase bilayers after 15 μs of unbiased simulation time using the standard MARTINI model.[36] While the authors did not elucidate the driving forces underlying this behavior, the results qualitatively agree with our study; it should be noted that the longer amphiphilic ligands studied also allow partial penetration into the bilayer, which is not observed for the short, charged ligands studied here. Another computational study performed using CG dissipative particle dynamics (DPD) simulations found that hydrophilic NPs cluster near phase boundaries.[54] These findings are again qualitatively consistent with our results, although it is challenging to directly compare the DPD model parameters to the more chemically specific MARTINI parameters. Based on the the competition between attractive NP-bilayer interactions and curvature free energy identified in this work, we anticipate that the interactions of collections of NPs with phase-separated bilayers could be simulated by incorporating the attractive interactions from the MARTINI simulations into even coarser simulation models that reproduce continuum elastic energies.[38] Such studies will be the subject of future work.

The curvature-driven interactions of NPs with the phase boundary suggests design guidelines for directing nanomaterial assembly on phase-separated bilayers. For example, tuning the diameter of the NP to match the radius of curvature of the phase boundary may further increase the number of NP-bilayer contacts without inducing unfavorable bilayer curvature, leading to a stronger driving force for boundary adsorption. We estimate that the radius of curvature, approximated by $1/H(x,y)$, of the one-phase L_d bilayer is 3.9 nm near the adsorbed NP, while the intrinsic radius of curvature in the y-direction at the interface of the L_d phase and the phase boundary (*i.e.*, at the PMF minimum in Fig. 6) is 8.9 nm. The difference in these values suggests that NPs larger than the 4 nm NP studied here may induce curvature that more closely matches the intrinsic curvature of the interface and thus may more strongly prefer the boundary. Similarly, nanorods with large aspect ratios may strongly prefer adsorbing to and aligning parallel to the phase boundary to match both radii of curvature of the nanorod to the intrinsic radii of curvature at the boundary. Similar arguments could also apply to peripheral proteins or peptides that adsorb to the bilayer surface. As a general design guideline, we thus predict that tuning the radii of curvature of a nanomaterial to match the intrinsic curvature at the phase boundary could enable the directed assembly of NPs at this topographical feature.

5 Conclusion

In this work, we performed classical molecular dynamics simulations using the coarse-grained MARTINI force field and the BMW water model to study the adsorption of a 4 nm cationic NP to lipid bilayers containing L_d and L_o domains. We first measured the free energy for adsorbing the NP to independent one-phase L_d and L_o bilayers and found that the NP adsorbs more strongly to the L_d bilayer. By measuring attractive Lennard-Jones interactions and approximating the elastic free energy penalty associated with induced bilayer curvature, we determined that adsorption to the L_d bilayer is preferred because curvature can be more easily induced to maximize favorable NP-bilayer contacts. Using the same modeling framework, we measured the free energy for moving a NP between the L_d and L_o domains in a phase-separated raft-like bilayer. These simulations revealed a local free energy minimum at the interface between the phase boundary and the L_d domain and a local free energy maximum at the interface between the phase boundary and the L_o domain. We again rationalized these results in terms of the competition between attractive NP-bilayer interactions and the penalty for inducing curvature. We specifically found that the intrinsic negative curvature present at the interface between the phase boundary and L_d domain leads to the local free energy minimum, while the intrinsic positive curvature at the interface between the phase boundary and the L_o domain leads to the local maximum. These results suggest that experimental observations of stronger NP adsorption to phase-separated bilayers relative to single-component bilayers may be due to a preference for the phase boundary. The results also indicate that the spatially heterogeneous composition of phase-separated lipid bilayers can directly affect NP adsorption and potentially assembly, which suggests new design rules for nanomaterials that interact with phase boundaries.

Conflicts of interest

There are no conflicts to declare.

Acknowledgements

JKS and RCV acknowledge support from the Department of Chemical and Biological Engineering at the University of Wisconsin-Madison and the Wisconsin Alumni Research Fund. This work used the Extreme Science and Engineering Discovery Environment (XSEDE), which is supported by National Science Foundation grant number ACI-1549562. The contributions of JAP were supported by the Center for Sustainable Nanotechnology, CHE-1503408.

Notes and references

1 X. Huang, P. K. Jain, I. H. El-Sayed and M. A. El-Sayed, *Nanomedicine*, 2007, **2**, 681–693.
2 X. Gao, Y. Cui, R. M. Levenson, L. W. K. Chung and S. Nie, *Nature Biotechnology*, 2004, **22**, 969–976.
3 P. Ghosh, G. Han, M. De, C. K. Kim and V. M. Rotello, *Advanced Drug Delivery Reviews*, 2008, **60**, 1307 – 1315.
4 T. Sun, Y. S. Zhang, B. Pang, D. C. Hyun, M. Yang and Y. Xia, *Angewandte Chemie International Edition*, 2014, **53**, 12320–12364.
5 M. Sun, F. Liu, Y. Zhu, W. Wang, J. Hu, J. Liu, Z. Dai, K. Wang, Y. Wei, J. Bai and W. Gao, *Nanoscale*, 2016, **8**, 4452–4457.
6 D. O'Neal, L. R. Hirsch, N. J. Halas, J. Payne and J. L. West, *Cancer Letters*, 2004, **209**, 171–176.

7 R. Mout, D. F. Moyano, S. Rana and V. M. Rotello, *Chem. Soc. Rev.*, 2012, **41**, 2539–2544.

8 A. Albanese, P. S. Tang and W. C. Chan, *Annual Review of Biomedical Engineering*, 2012, **14**, 1–16.

9 A. M. Alkilany, S. E. Lohse and C. J. Murphy, *Accounts of Chemical Research*, 2013, **46**, 650–661.

10 S. Behzadi, V. Serpooshan, W. Tao, M. A. Hamaly, M. Y. Alkawareek, E. C. Dreaden, D. Brown, A. M. Alkilany, O. C. Farokhzad and M. Mahmoudi, *Chemical Society Reviews*, 2017, **46**, 4218–4244.

11 A. Verma and F. Stellacci, *Small*, 2010, **6**, 12–21.

12 A. E. Nel, L. Mädler, D. Velegol, T. Xia, E. M. V. Hoek, P. Somasundaran, F. Klaessig, V. Castranova and M. Thompson, *Nature Materials*, 2009, **8**, 543–557.

13 Y. Jiang, S. Huo, T. Mizuhara, R. Das, Y.-W. Lee, S. Hou, D. F. Moyano, B. Duncan, X.-J. Liang and V. M. Rotello, *ACS Nano*, 2015, **9**, 9986–9993.

14 A. Verma, O. Uzun, Y. Hu, Y. Hu, H.-S. Han, N. Watson, S. Chen, D. J. Irvine and F. Stellacci, *Nature materials*, 2008, **7**, 588.

15 C. M. Jewell, J.-M. Jung, P. U. Atukorale, R. P. Carney, F. Stellacci and D. J. Irvine, *Angewandte Chemie International Edition*, 2011, **50**, 12312–12315.

16 S. Li and N. Malmstadt, *Soft Matter*, 2013, **9**, 4969–4976.

17 C. M. Goodman, C. D. McCusker, T. Yilmaz and V. M. Rotello, *Bioconjugate Chemistry*, 2004, **15**, 897–900.

18 Y.-C. Yeh, B. Creran and V. M. Rotello, *Nanoscale*, 2012, **4**, 1871–1880.

19 R. C. Van Lehn, M. Ricci, P. H. Silva, P. Andreozzi, J. Reguera, K. Voïtchovsky, F. Stellacci and A. Alexander-Katz, *Nature Communications*, 2014, **5**, 4482.

20 A. Lesniak, A. Salvati, M. J. Santos-Martinez, M. W. Radomski, K. A. Dawson and C. ÃĚberg, *Journal of the American Chemical Society*, 2013, **135**, 1438–1444.

21 B. Y. Moghadam, W.-C. Hou, C. Corredor, P. Westerhoff and J. D. Posner, *Langmuir*, 2012, **28**, 16318–16326.

22 E. S. Melby, S. E. Lohse, J. E. Park, A. M. Vartanian, R. A. Putans, H. B. Abbott, R. J. Hamers, C. J. Murphy and J. A. Pedersen, *ACS Nano*, 2017, **11**, 5489–5499.

23 J. M. Troiano, L. L. Olenick, T. R. Kuech, E. S. Melby, D. Hu, S. E. Lohse, A. C. Mensch, M. Dogangun, A. M. Vartanian, M. D. Torelli, E. Ehimiaghe, S. R. Walter, L. Fu, C. R. Anderton, Z. Zhu, H. Wang, G. Orr, C. J. Murphy, R. J. Hamers, J. A. Pedersen and F. M. Geiger, *The Journal of Physical Chemistry C*, 2015, **119**, 534–546.

24 Y. Guo, E. Terazzi, R. Seemann, J. B. Fleury and V. A. Baulin, *Science Advances*, 2016, **2**, e1600261.

25 P. U. Atukorale, Z. P. Guven, A. Bekdemir, R. P. Carney, R. C. Van Lehn, D. S. Yun, P. H. Jacob Silva, D. Demurtas, Y.-S. Yang, A. Alexander-Katz *et al.*, *Bioconjugate chemistry*, 2018, **29**, 1131–1140.

26 F. Franz, C. Aponte-Santamaría, C. Daday, V. Miletić and F. Gräter, *The Journal of Physical Chemistry B*, 2018, **122**, 7073–7079.

27 M. Ramezanpour, S. Leung, K. Delgado-Magnero, B. Bashe, J. Thewalt and D. Tieleman, *Biochimica et Biophysica Acta (BBA) - Biomembranes*, 2016, **1858**, 1688–1709.

28 E. Heikkilä, H. Martinez-Seara, A. A. Gurtovenko, M. Javanainen, H. Häkkinen, I. Vattulainen and J. Akola, *The Journal of Physical Chemistry C*, 2014, **118**, 11131–11141.

29 P. Angelikopoulos, L. Sarkisov, Z. Cournia and P. Gkeka, *Nanoscale*, 2017, **9**, 1040–1048.

30 H. Chan and P. KraĺL, *ACS Omega*, 2018, **3**, 10631–10637.

31 P. A. Oroskar, C. J. Jameson and S. Murad, *Langmuir*, 2016, **32**, 7541–7555.

32 S. Pogodin, M. Werner, J.-U. Sommer and V. A. Baulin, *Acs Nano*, 2012, **6**, 10555–10561.

33 S. Salassi, F. Simonelli, D. Bochicchio, R. Ferrando and G. Rossi, *The Journal of Physical Chemistry C*, 2017, **121**, 10927–10935.

34 E. M. Curtis, A. H. Bahrami, T. R. Weikl and C. K. Hall, *Nanoscale*, 2015, **7**, 14505–14514.

35 J. Lin, H. Zhang, Z. Chen and Y. Zheng, *ACS Nano*, 2010, **4**, 5421–5429.

36 X. Chen, D. P. Tieleman and Q. Liang, *Nanoscale*, 2018, **10**, 2481–2491.

37 K. Xiong, J. Zhao, D. Yang, Q. Cheng, J. Wang and H. Ji, *Soft Matter*, 2017, **13**, 4644–4652.

38 A. Šarić and A. Cacciuto, *Soft Matter*, 2013, **9**, 6677.

39 M. Edidin, *Nature Reviews Molecular Cell Biology*, 2003, **4**, 414–418.

40 D. Lingwood and K. Simons, *Science (New York, N.Y.)*, 2010, **327**, 46–50.

41 G. W. Feigenson, *Biochimica et Biophysica Acta (BBA) - Biomembranes*, 2009, **1788**, 47–52.

42 S. Munro, *Cell*, 2003, **115**, 377 – 388.

43 E. Sezgin, I. Levental, S. Mayor and C. Eggeling, *Nature Reviews Molecular Cell Biology*, 2017, **18**, 361.

44 L. Toppozini, S. Meinhardt, C. L. Armstrong, Z. Yamani, N. Kučerka, F. Schmid and M. C. Rheinstädter, *Physical Review Letters*, 2014, **113**, 228101.

45 R. D. Usery, T. A. Enoki, S. P. Wickramasinghe, V. P. Nguyen, D. G. Ackerman, D. V. Greathouse, R. E. Koeppe, F. N. Barrera and G. W. Feigenson, *Biophysical Journal*, 2018, **114**, 2152 – 2164.

46 G. Khelashvili, B. Kollmitzer, P. Heftberger, G. Pabst and D. Harries, *Journal of Chemical Theory and Computation*, 2013, **9**, 3866–3871.

47 E. S. Melby, A. C. Mensch, S. E. Lohse, D. Hu, G. Orr, C. J. Murphy, R. J. Hamers and J. A. Pedersen, *Environmental Science: Nano*, 2016, **3**, 45–55.

48 T. Hamada, M. Morita, M. Miyakawa, R. Sugimoto, A. Hatanaka, M. C. Vestergaard and M. Takagi, *Journal of the American Chemical Society*, 2012, **134**, 13990–13996.

49 S. M. Maté, R. F. Vázquez, V. S. Herlax, M. A. Daza Millone, M. L. Fanani, B. Maggio, M. E. Vela and L. S. Bakás, *Biochimica et Biophysica Acta (BBA) - Biomembranes*, 2014, **1838**, 1832–1841.

50 S.-T. Yang, V. Kiessling, J. A. Simmons, J. M. White and L. K. Tamm, *Nature Chemical Biology*, 2015, **11**, 424–431.

51 W. Rawicz, B. A. Smith, T. J. McIntosh, S. A. Simon and E. Evans, *Biophysical journal*, 2008, **94**, 4725–36.

52 K. H. Sheikh and S. P. Jarvis, *Journal of the American Chemical Society*, 2011, **133**, 18296–18303.

53 P. I. Kuzmin, S. A. Akimov, Y. A. Chizmadzhev, J. Zimmerberg and F. S. Cohen, *Biophysical journal*, 2005, **88**, 1120–33.

54 D. L. Cheung, *The Journal of Chemical Physics*, 2014, **141**, 194908.

55 S. J. Marrink, H. J. Risselada, S. Yefimov, D. P. Tieleman and A. H. de Vries, *The Journal of Physical Chemistry B*, 2007, **111**, 7812–7824.

56 E. L. da Rocha, G. F. Caramori and C. R. Rambo, *Phys. Chem. Chem. Phys.*, 2013, **15**, 6801.

57 S. J. Marrink and D. P. Tieleman, *Chemical Society Reviews*, 2013, **42**, 6801.

58 Z. Wu, Q. Cui and A. Yethiraj, *Journal of Chemical Theory and Computation*, 2011, **7**, 3793–3802.

59 Z. Wu, Q. Cui and A. Yethiraj, *The Journal of Physical Chemistry B*, 2013, **117**, 12145–12156.

60 H. J. Risselada and S. J. Marrink, *Proceedings of the National Academy of Sciences*, 2008, **105**, 17367–17372.

61 R. S. Davis, P. B. Sunil Kumar, M. M. Sperotto and M. Laradji, *The Journal of Physical Chemistry B*, 2013, **117**, 4072–4080.

62 S. Pronk, S. Páll, R. Schulz, P. Larsson, P. Bjelkmar, R. Apostolov, M. R. Shirts, J. C. Smith, P. M. Kasson, D. van der Spoel, B. Hess and E. Lindahl, *Bioinformatics*, 2013, **29**, 845–854.

63 L. Monticelli, S. K. Kandasamy, X. Periole, R. G. Larson, D. P. Tieleman and S.-J. Marrink, *Journal of Chemical Theory and Computation*, 2008, **4**, 819–834.

64 J. Hong, R. J. Hamers, J. A. Pedersen and Q. Cui, *The Journal of Physical Chemistry C*, 2017, **121**, 3584–3596.

65 T. A. Wassenaar, H. I. Ingólfsson, R. A. Böckmann, D. P. Tieleman and S. J. Marrink, *Journal of Chemical Theory and Computation*, 2015, **11**, 2144–2155.

66 J. S. Hub, B. L. de Groot and D. van der Spoel, *Journal of Chemical Theory and Computation*, 2010, **6**, 3713–3720.

67 J. D. Nickels, X. Cheng, B. Mostofian, C. Stanley, B. Lindner, F. A. Heberle, S. Perticaroli, M. Feygenson, T. Egami, R. F. Standaert, J. C. Smith, D. A. A. Myles, M. Ohl and J. Katsaras, *Journal of the American Chemical Society*, 2015, **137**, 15772–15780.

68 Z. Chen and R. Rand, *Biophysical Journal*, 1997, **73**, 267 – 276.

69 B. Seguin and E. Fried, *Journal of Mathematical Biology*, 2014, **68**, 647–665.

70 C. Yolcu, R. C. Haussman and M. Deserno, *Advances in Colloid and Interface Science*, 2014, **208**, 89–109.

71 M. M. Kozlov and W. Helfrich, *Langmuir*, 1992, **8**, 2792–2797.

72 T. Baumgart, B. R. Capraro, C. Zhu and S. L. Das, *Annual Review of Physical Chemistry*, 2011, **62**, 483–506.

73 T. R. Kuech, *Ph.D. thesis*, University of Wisconsin-Madison, 2015.

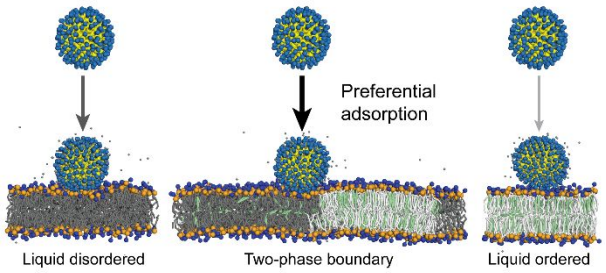

Coarse-grained molecular dynamics simulations and free energy calculations reveal that cationic nanoparticles preferentially adsorb to regions of intrinsic negative curvature at phase boundaries in multicomponent lipid bilayers.